Progress In Electromagnetics Research M, Vol. 125, 31-40, 2024

PIER M

(Received 22 January 2024, Accepted 29 February 2024, Scheduled 11 March 2024)

# Electromagnetic-Thermal Modeling of Multi-Turn Electromagnetic Rail Launcher with Phase Transition

Jian Sun[1,2], Ling Xiong[2], Yuantao Cong[1,2], and Junsheng Cheng[1,2,3,*]

[1] *University of Chinese Academy of Sciences, Beijing 100049, China*
[2] *Institute of Electrical Engineering, Chinese Academy of Sciences, Beijing 100190, China*
[3] *Institute of Electrical Engineering and Advanced Electromagnetic Drive Technology, Qilu Zhongke, Jinan, China*

**ABSTRACT:** Electromagnetic thermal performance is critical during electromagnetic launch. However, due to the harsh in-bore environment, it is difficult to obtain multi-parameter information by means of experimental measurement, which further limits our understanding of the field distribution of electromagnetic launcher. In this paper, considering the temperature dependence of material conductivity and armature solid-liquid isothermal phase transition, a bidirectional coupling model of electro-magnetic-thermal field of multi-turn electromagnetic rail launcher is established. The reliability of this model is verified by comparing the calculation results of the same model and input conditions with the numerical tool EMAP3D, as well as the related experimental comparison. In addition, the multi-turn and traditional EMRLs are compared and analyzed. The results show that compared to single-turn EMRL, the armatures have greater driving force in two multi-turn configurations, and the impulse lifting rates are about 1/2. In the multi-turn configurations, the lateral resultant forces of the two armatures are not zero, while the lateral force difference in the integrated negative rail configuration is relatively small. The ablation of the armature in the integrated negative rail configuration is less severe.

## 1. INTRODUCTION

In recent years, electromagnetic rail launcher (EMRL) that utilizes electromagnetic energy to the motion of an object has been extensively studied because of its unparalleled advantages. Compared with traditional chemical propulsion systems, EMRL can break through the limitation of lagging sound velocity and accelerate the armature to more than 3000 m/s [1]. EMRL has the advantages of full electric control and low pollution [2, 3]. Under extreme physical conditions such as high current density and high temperature, the conductor temperature rises rapidly, and the conductor materials undergo a transition from solid to liquid phase, and even vaporization [4–6]. This will lead to a deterioration of the in-bore environment, and ultimately the overall performance and service life of EMRL will be destroyed [7, 8]. Therefore, accurate acquisition and understanding of the evolution of magnetic fields, currents, and thermal fields in rail and armature are critical to improving the durability of EMRL.

Previous studies have contained a large number of schemes for electromagnetic and thermal field calculations. Bayati et al. used IEM time domain method to predict current distribution and maximum current density [9], and calculate the thermal distribution on the surface and surrounding of the rail [10]. Pang et al. used the Peaceman-Rachford differential format to numerically discretize the electromagnetic control equations of EMRL and obtained the distribution of the two-dimensional armature and rail electromagnetic field with the effect of velocity skin effect [11]. Gong and Weng used the Douglas-Brian finite difference format to develop a three-dimensional numerical model of current melt-wave erosion (MWE) [12]. With the advancement of numerical simulation technology, some characteristic finite element algorithms are proposed, which has greatly promoted the development of electromagnetic launch science. Based on the Lagrange formula, Hsieh developed the railgun program ‘EMAP3D’ for mechanical and thermally coupled electromagnetic diffusion processes [13]. Using the common code ANSYS as the base calculation engine, Shatoff et al. developed the mobile armature railgun code (called HERB) for coupling electromagnetic, thermal and structural fields [14]. Lin and Li used a finite element and boundary element hybrid algorithm to develop a transient multiphysics solver [15].

Most of the previous modeling work is based on the traditional EMRL or augmented EMRL of hexahedral meshes. However, hexahedral meshes are difficult to generate models with complex conductor geometries and surrounding air regions. This makes the conductor topology need to be adjusted appropriately for easy modeling. More importantly, the properties of solid metals continue to change significantly with high temperatures, and the phase transition process is not considered.

In this paper, considering the temperature dependence of material conductivity and armature solid-liquid isothermal phase transition, a bidirectional coupling model of electro-magnetic-thermal field of multi-turn EMRL is established. The model is based on tetrahedral meshes and accommodates multiple configurations of conductors and air domains. The reliability of this model is verified by comparing the calculation results of the same model and input conditions with the numerical tool EMAP3D, as well as the related experimental comparison. In addition, two kinds of multi-turn EMRLs and traditional EMRL are compared and analyzed.

---

* Corresponding author: Junsheng Cheng (jscheng@mail.iee.ac.cn).

doi:10.2528/PIERM24012204

Published by THE ELECTROMAGNETIC ACADEMY

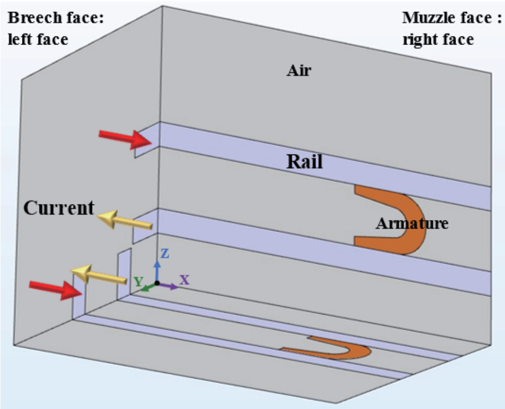

**FIGURE 1.** Schematic diagram of a typical 1/4 physical model.

## 2. THEORY OF ELECTRO-MAGNETIC-THERMAL FIELD COUPLING ANALYSIS IN EMRLS

### 2.1. Equations for the Electromagnetic Field

The vector magnetic potential A and scalar electric potential $\varphi$ are used to solve the electromagnetic field governing equation of the EMRL. The uniform form of the electromagnetic field control equation of EMRL can be written as Eqs. (1) and (2):

$$\nabla \times \frac{1}{\mu} \nabla \times \mathbf{A} + \sigma \left( \nabla \varphi + \frac{\partial \mathbf{A}}{\partial t} \right) = 0 \tag{1}$$

$$\nabla \cdot \left( -\sigma \nabla \varphi - \sigma \frac{\partial \mathbf{A}}{\partial t} \right) = 0 \tag{2}$$

where $\mu$ is the magnetic permeability, $\sigma$ the electrical conductivity, and $t$ the time.

To ensure the symmetry of the coefficient matrix, a time-integrated scalar potential $\Phi$ is introduced.

$$\Phi = \int_0^t \varphi dt \tag{3}$$

Substituting Eq. (3) into Eqs. (1) and (2), the Coulomb gauge is imposed in the form of penalty function, then the Galerkin format of the electromagnetic field equations are obtained:

$$\begin{aligned} &\int_V \left( \frac{1}{\mu} \nabla \times \mathbf{W}_j \cdot \nabla \times \mathbf{A} + \frac{1}{\mu} \nabla \cdot \mathbf{W}_j \nabla \cdot \mathbf{A} \right. \\ &\left. + \sigma \mathbf{W}_j \cdot \frac{\partial}{\partial t} \nabla \Phi + \sigma \mathbf{W}_j \cdot \frac{\partial \mathbf{A}}{\partial t} \right) dV = 0 \end{aligned} \tag{4}$$

$$\int_V \nabla W_j \cdot \left( \sigma \nabla \frac{\partial \phi}{\partial t} + \sigma \frac{\partial \mathbf{A}}{\partial t} \right) dV = 0 \tag{5}$$

where $\mathbf{W}$ is the vector weight function, and $W$ is the scalar weight function. In order for the mesh to adapt well to the complex structural conductors as well as the surrounding air domain, the 4-node tetrahedral elements are used to mesh the solution domain.

The boundary conditions of different media need to satisfy the continuity of the tangential component of the electric field **E**, the continuity of the normal component of the current density **J**, the continuity of the tangential component of the magnetic field intensity **H**, and the continuity of the normal component of the magnetic induction intensity **B**.

A quarter of the structure (see Fig. 1) is taken as the computational domain because of symmetry. For each turn of multi-turn EMRL, the excitation current flows in from the tail end of one rail, flows through the armature, and then flows out of the tail end of the other rail. Red arrows represent current flowing into of the rails, and yellow arrows represent current flowing out the rails. The electromagnetic fields of conductors between different turns influence each other.

The breech face and muzzle face belong to the boundary $S_B$ and satisfy $\mathbf{A} \times \mathbf{n} = 0$. Considering the symmetry of the model, the symmetric boundaries $S_H$ ($\mathbf{A} \cdot \mathbf{n} = 0$) [16] are used on the $Z = 0$ plane and $Y = 0$ plane to reduce the amount of calculation. Using the commonly used means in finite element electromagnetic calculation, the remaining envelope surface of the air domain is set to $S_\infty$ boundary ($\mathbf{A} = 0$), and zero vector magnetic potential will result in a certain truncation error.

According to the boundary conditions of the electromagnetic field, the current inflow and outflow end faces need to satisfy that the tangential component of the current is zero, which means $\varphi = constant$. For breech face where the current flows out (yellow arrows), the scalar potential $\varphi$ is specified to be zero for reference. For the breech face where the current flows in (red arrows), scalar potential $\varphi$ is the value that changes over time. The corresponding value at each time needs to be tried twice: $\varphi_1 \xrightarrow{\text{calculate}} I_{\text{trial 1}}$ and $\varphi_2 \xrightarrow{\text{calculate}} I_{\text{trial 2}}$. Then, it is obtained by linear interpolation $((\varphi_t = \varphi_1 + (I_{\text{given}} - I_{\text{trial 1}})\, \varphi_2 - \varphi_1 / I_{\text{trial 2}} - I_{\text{trial 1}}))$ of the previous two attempts to meet the requirements of the given current. Furthermore, the value of $\varphi$ needs to be further converted into $\Phi$ according to Eq. (3).

All boundaries belong to the Dirichlet boundary, so they can be quickly implemented by simply processing the matrix.

The backward Euler method (implicit) is used for numerical discretization.

$$\left[\mathbf{K}+\frac{\mathbf{M}}{\Delta t}\right]\left[\mathbf{A}_{\phi}^{t+\Delta t}\right]=\left[\frac{\mathbf{M}}{\Delta t}\right]\left[\mathbf{A}_{\phi}^{t}\right] \tag{6}$$

where $\mathbf{K}$ is the stiffness matrix; $\mathbf{M}$ is the damping matrix; and $\mathbf{A}_{\Phi}^{t+\Delta t}$ are the unknown quantities at the current time and $\mathbf{A}_{\Phi}^{t}$ the previous time, respectively.

The calculated dual-potential solutions require further post-processing to obtain the corresponding field distribution results. The electromagnetic force formed by the interaction between the armature current and the magnetic field between the rails can be described as:

$$\mathbf{F}=\int_{V}\mathbf{J}\times\mathbf{B}dV \tag{7}$$

## 2.2. Equations for the Thermal Field

The equation of the thermal field is based on heat conduction Eq. (8), in which $T$ is the temperature, $\rho$ the mass density, $c$ the specific heat, $\lambda$ the thermal conductivity, and $Q_S$ the energy absorbed per unit volume and time during melting

$$\rho c\frac{\partial T}{\partial t}-\nabla\cdot\lambda\nabla T=\frac{J^2}{\sigma}-Q_S \tag{8}$$

$$Q_s=\begin{cases}0,\ (T<T_m)\\ \frac{\partial E_s}{\partial t},\ E_s=\int_{T_m}^{T}\rho c dT,\ (T\geq T_m)\end{cases} \tag{9}$$

At the same time, the temperature dependence of electrical conductivity is considered. Compared to the conductor's own ohmic heating, the heat convection between the conductor and the air is negligible, so the interface is regarded as an adiabatic surface. The temperature values on two sides of the rail-armature interface are equal.

Similarly, in three dimensions, the heat conduction equation can be expressed as:

$$\left[\mathbf{K_T}+\frac{\mathbf{M_T}}{\Delta t}\right]\left[\mathbf{T}^{t+\Delta t}\right]=\left[\frac{\mathbf{M_T}}{\Delta t}\right]\left[\mathbf{T}\right]^{t}+\left[\mathbf{Q}_{\mathbf{T}}^{t+\Delta t}\right] \tag{10}$$

where $\mathbf{K_T}$ is the temperature field stiffness matrix; $\mathbf{M_T}$ is the temperature field damping matrix; $\mathbf{Q}_{\mathbf{T}}^{t+\Delta t}$ is the heat source term matrix; $\mathbf{T}^{t+\Delta t}$ and $\mathbf{T}^{t}$ are the temperatures at the current time and the previous time, respectively.

## 2.3. The Coupled Analysis of the Multi-Field

During the discharge of pulsed high currents, ohmic heating causes the conductor temperature to rise. The electrical conductivity of the conductor decreases with the increase of temperature, which in turn affects the solution of the electromagnetic field, forming a bidirectional coupling.

In this paper, the calculation of the thermal field takes into account the isothermal phase transition process based on node ablation method, which approximates the transition from solid to liquid by adjusting the conductivity of the ablation node. The armature material has a low melting point, and once the local temperature of the armature reaches its melting temperature ($T_m$), the armature material begins to melt. When the calculated temperature is higher than the melting temperature of the armature material, it will be forced to become the melting temperature. This operation results in energy loss, which is obtained by Eq. (9). For all time steps, the cumulative amount of the energy loss ($\sum E_s$) is the equivalent latent heat energy used to transition phases. The phase transition process ends when the accumulated energy reaches the energy required for fusion latent heat ($\rho H_L$). Finally, the molten material is transformed from solid to liquid. According to the calculation experience, it is found that more accurate results can be obtained when the conductivity at the melting temperature is reduced by 4 orders of magnitude [17]. The above analysis can be shown with Fig. 2 in detail, and this code is implemented by Matlab software.

## 3. VERIFICATION OF MULTI-FIELD COUPLING CALCULATION METHOD

In order to verify the correctness of the established EMRL multi-field coupling calculation method, the same simple EMRL model and input conditions as in [13] are calculated, and the calculation results are compared with EMAP3D.

The armature is a block of 6 mm×3 mm×3 mm, and the rail is a block of 40 mm×6 mm×3 mm. The armature and rail material properties are shown in Table 1.

As shown in Fig. 3, the current waveform calculated in this paper is in good agreement with the current waveform calculated by EMAP3D. In addition, the maximum temperature of the armature at 0.72 ms calculated in this paper is about 38.2°C, and the temperature calculated by EMAP3D is about 40.7°C. The relative error is about 6.14%, which is controlled within a satisfactory range.

In addition, we conducted a related test to verify the developed code. A high-frequency high-precision 3D magnetic probe is used to measure the magnetic field at the observation point, and the calculation results and measurement results are shown in Fig. 4. Overall, the error is controlled within a reasonable range. Fig. 5 shows a comparison of currents, where the measured current is obtained through a Rogowski coil, and the calculated current is the current density integral value of the rail section. The two maintain good consistency.

Thus, the electro-magnetic-thermal multiphysics coupling code developed in this paper is valid.

## 4. FINITE ELEMENT MODELS OF MULTI-TURN EMRLS

Figure 6 shows the armature geometric dimensions and three different configuration types of EMRLs and their current directions. Configuration 1 is a simple EMRL, while configurations 2 and 3 are four-turn EMRLs in a circular array. All rectangular section rails are 30 mm×8 mm in size. The negative rails in configuration 3 are integrated. A through hole with a radius of 19.4 mm is dug in the middle of the negative rail in configuration 3 to ensure that its area is equal to four positive rails.

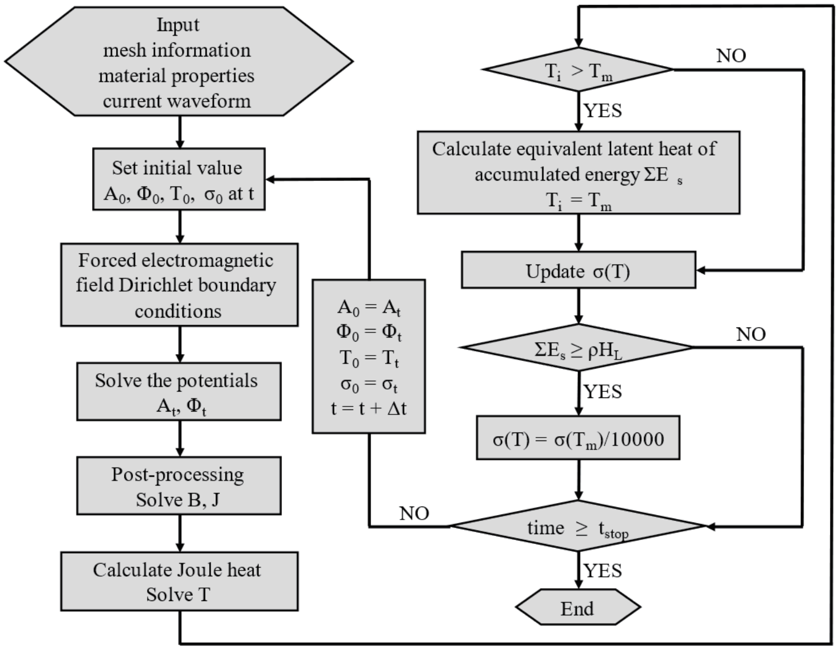

**FIGURE 2**. The computation flowchart of the multi-field model.

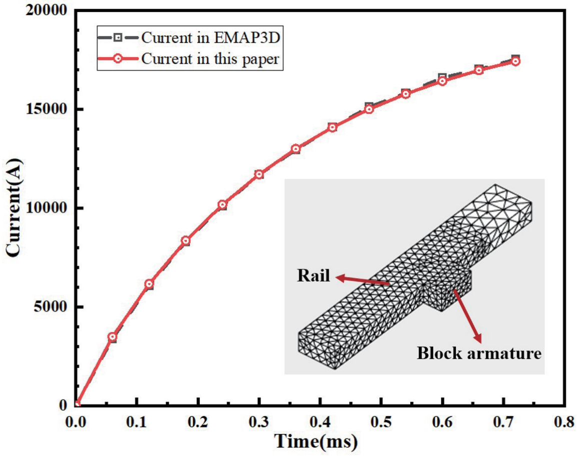

**FIGURE 3**. Comparison of current waveforms under block armature.

**TABLE 1**. Material parameters.

| Parameters | Copper alloy | Aluminum alloy |
|---|---|---|
| $\sigma_0/\mathrm{MS{\cdot}m^{-1}}$, initial electrical conductivity | 42 | 19 |
| $\mu/\mathrm{H{\cdot}m^{-1}}$, magnetic permeability | 1.2566e-6 | 1.2566e-6 |
| $\rho/\mathrm{kg{\cdot}m^{-3}}$, mass density | 8940 | 2700 |
| $\mathrm{c/J{\cdot}(kg{\cdot}K)^{-1}}$, specific heat | 390 | 880 |
| $\lambda/\mathrm{W{\cdot}(m{\cdot}K)^{-1}}$, thermal conductivity | 400 | 237 |
| $\alpha/\mathrm{K}$, temperature coefficient of resistivity | 0.0039 | 0.0042 |
| $\mathrm{T_m/K}$, melting point | $> 933.15$ | 933.15 |
| $\mathrm{H_L/kJ{\cdot}kg^{-1}}$, latent heat of fusion | — | 386.9 |

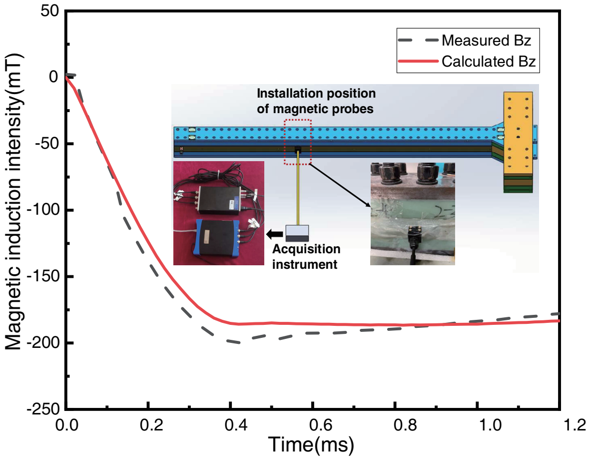

FIGURE 4. Magnetic field comparison.

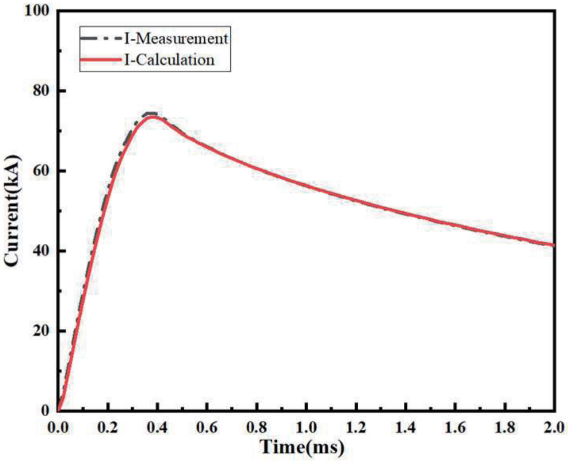

FIGURE 5. Current comparison.

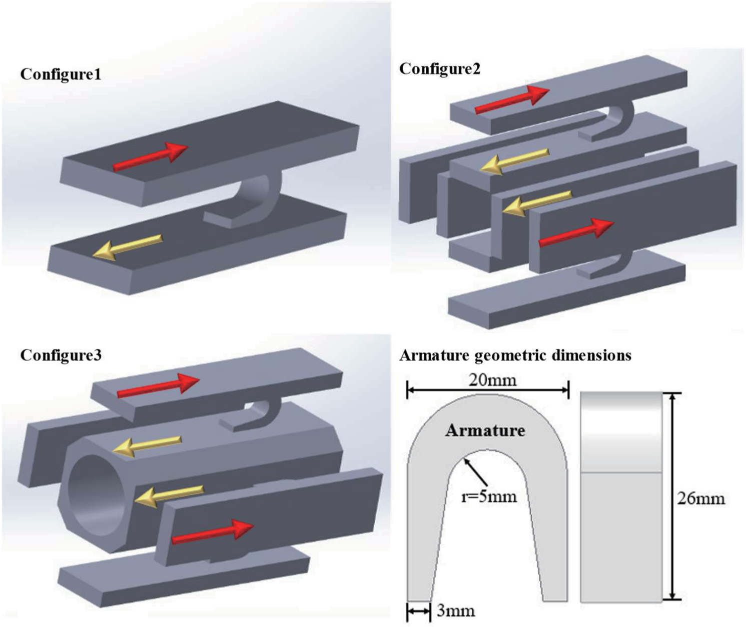

FIGURE 6. Armature geometric dimensions and different configurations of EMRLs.

This paper extends the design ideas of novel multi-turn EMRLs, rather than being limited to the described configurations. By properly distributing the angle of the circular array, EMRL structures such as 6 turns, 8 turns, and even more can be designed.

A flat-top pulse current is input to each turn of the rail as an excitation. The current reaches 450 kA at 0.4 ms. The current decays from 1.4 ms and drops to 100 kA at 2 ms. The time step is set to 0.04 ms during calculation.

## 5. FINITE ELEMENT CALCULATION AND ANALYSIS OF MULTI-TURN EMRLS

Using the material parameters in Table 1, the electromagnetic and thermal characteristics of EMRL in three configurations are calculated and discussed.

### 5.1. Electromagnetic Field Analysis

At 0.4 ms, the magnetic induction intensity distribution in the three configurations is shown in Fig. 7. Due to the skin effect, the magnetic induction intensity is concentrated on the surface of the conductor, and the armature laryngeal magnetic field is maximum. The corresponding armature magnetic induction intensity maximums in the three configurations are 23.55 T, 26.73 T, and 26.62 T, respectively. For multi-turn configurations, the magnetic induction intensity of the armature between different turns is mutually reinforcing, so the maximum magnetic induction intensity of the armature is larger than that of a single turn. In addition, for configurations 2 and 3, there is a self-shielding effect of the magnetic field in the space region enclosed by the negative rails. This phenomenon is shown by magnetic induction intensity distribution of the slice where the armature head is located (see Fig. 8). An approximately circu-

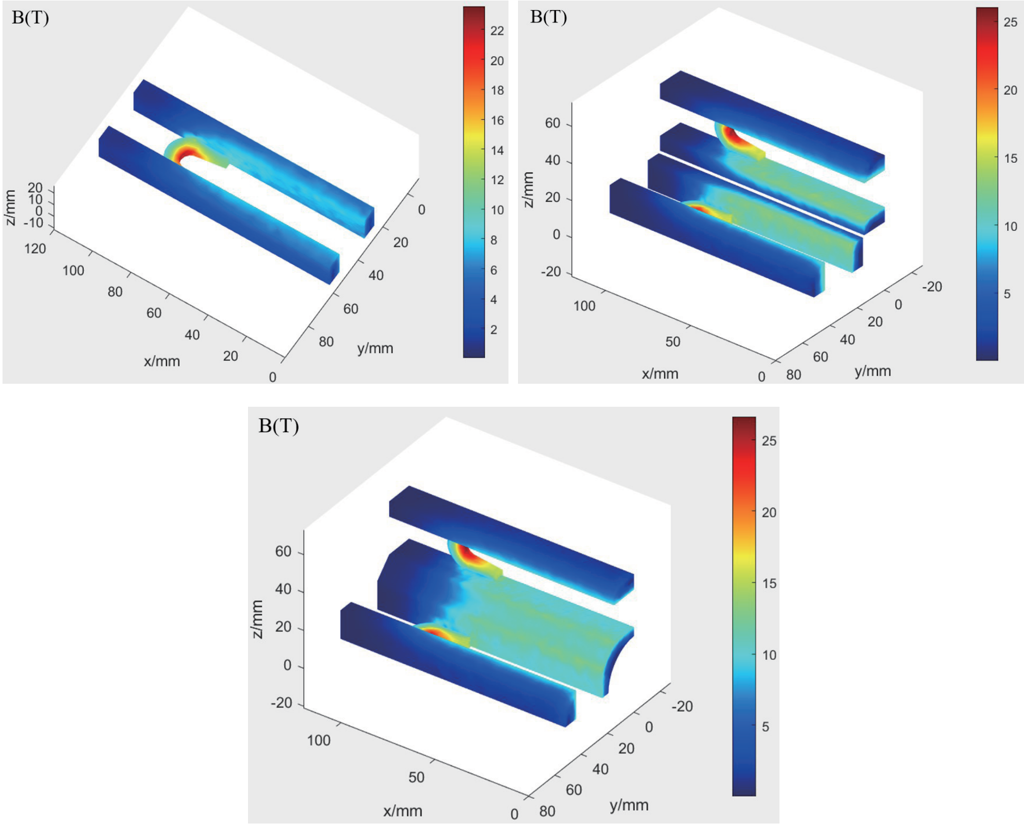

**FIGURE 7**. Magnetic induction intensity distribution at 0.4 ms under different configurations.

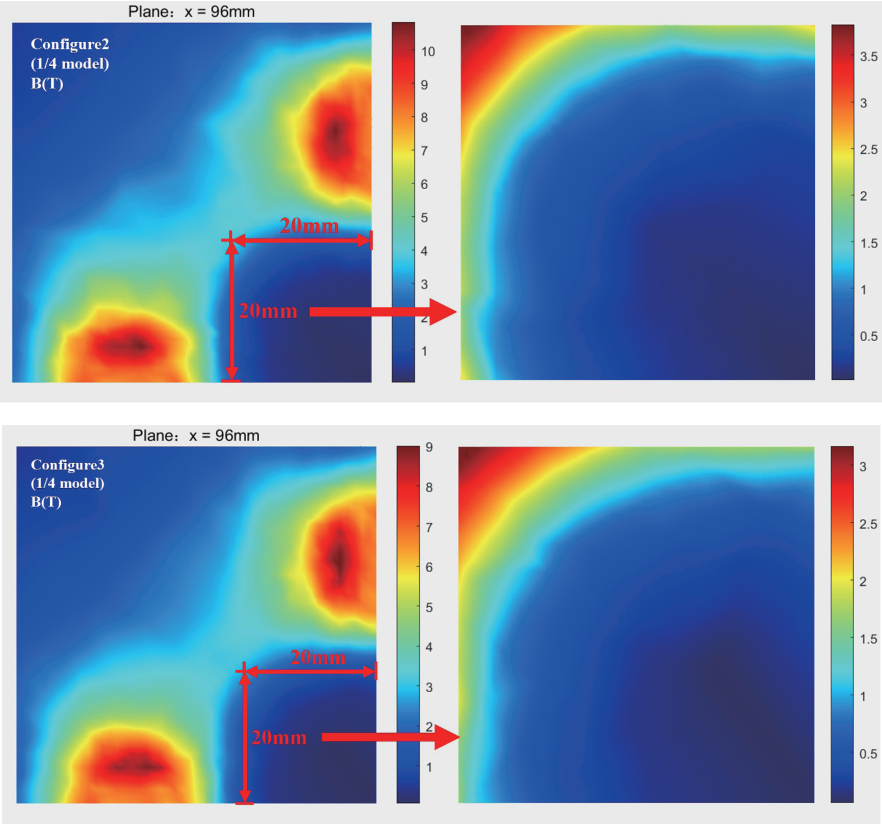

**FIGURE 8**. Magnetic induction intensity distribution at 1.4 ms for armature head section of configurations 2 and 3.

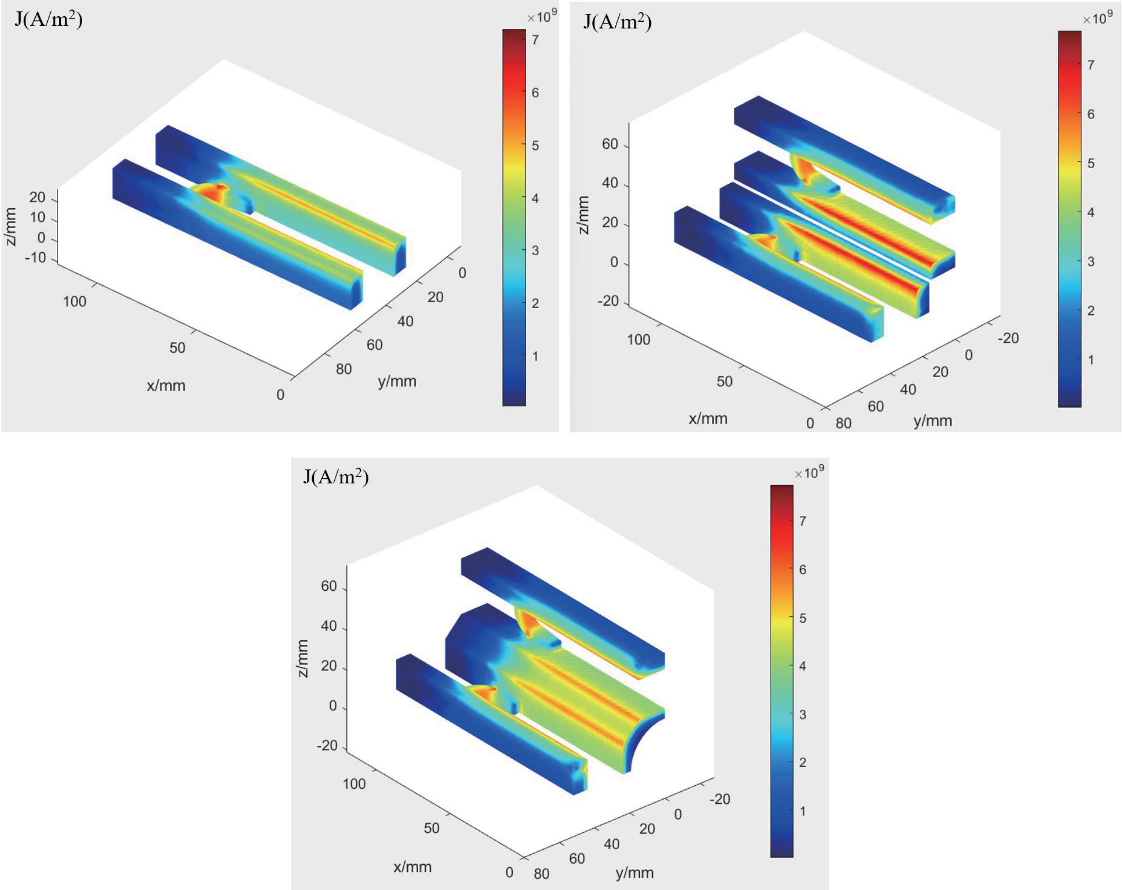

**FIGURE 9**. Current density distribution at 0.4 ms under different configurations.

lar magnetic field shielding area is formed. In the future, for the split negative rails, the multiple pairs of armatures can be designed to accelerate large mass load, and this self-shielding effect can effectively protect the electronic components inside the load.

Figure 9 shows the distribution of current densities at 0.4 ms for the three configurations. In addition to the armature throat, the current density at the leading edge of the contact between the armature and the rail and at the edge of the rail is relatively concentrated. Due to the symmetry of the structure, the current distributions of the positive and negative rails in configuration 1 are basically the same. However, the current density distributions of the positive and negative rail edges in configuration 2 are significantly different.

## 5.2. Mechanical Analysis

The electromagnetic driving force of the armature in the three configurations is shown in Fig. 10. The multi-turn configurations effectively increase the electromagnetic driving force carried by the armature, thereby improving the launch efficiency of the system. Impulse is used to quantify this efficiency gain. The integrals of electromagnetic driving force to time in the three configurations are 32.77 N·s, 49.40 N·s, and 46.09 N·s, respectively. As a result, the armature can acquire larger velocity. Compared with single-turn rails, the impulse lift rates in the two multi-turn configurations are 50.75% and 40.65%, respectively. In addition, in the flat-top phase of the current waveform, the driving force as a whole shows a trend of first decreasing and then slightly rising. This may be due to an increase in the temperature of the armature over time, which in turn decreases conductivity, increases the penetration depth ($\delta = \sqrt{\pi t/\sigma\mu}$) of the physics field, and finally the field is more evenly distributed.

During electromagnetic launch process, there is a contact pressure between the rear arm of the C-type armature and the rail, and this lateral force makes the contact pair fit closely. For single-turn electromagnetic rail launcher, the lateral resultant force of the armature is generally close to zero, which is determined by the symmetry of the structure. It is worth noting that in the multi-turn configurations, the lateral forces of the two rear arms of the armature tend to be different. As can be seen from Fig. 11, for configurations 2 and 3, the lateral resultant force of the armature is basically less than zero, which means that the contact pressure of the rear arm of the armature with the negative rail is greater than that with the positive rail. Excessively large lateral force differences are detrimental to the launch process and may lead to contact failures, which in turn affect the launch accuracy. The peak lateral resultant force of configuration 3 is $-857.33$ N, which is only 49.08% of configuration 2, so this is more conducive to the successful launch process than configuration 2.

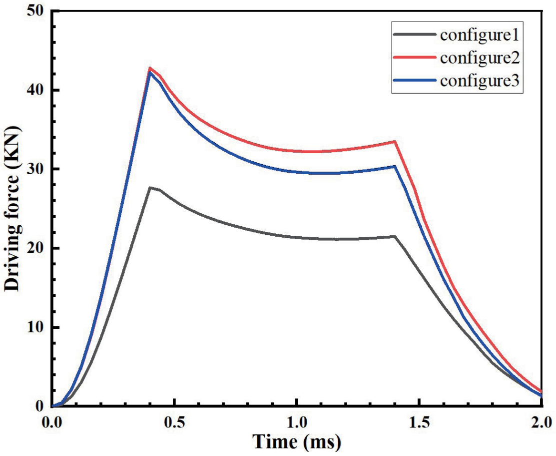

**FIGURE 10**. Comparison of electromagnetic driving forces.

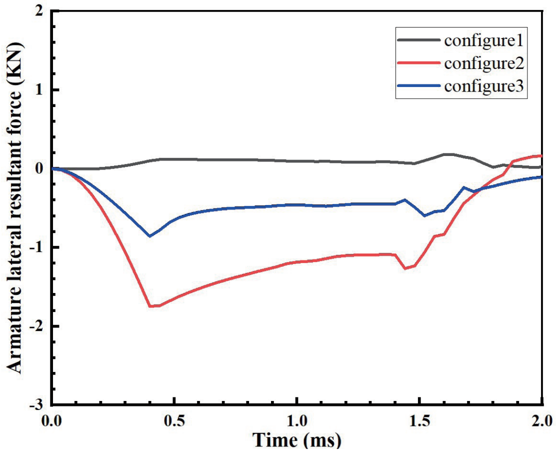

**FIGURE 11**. Comparison of armature lateral resultant forces.

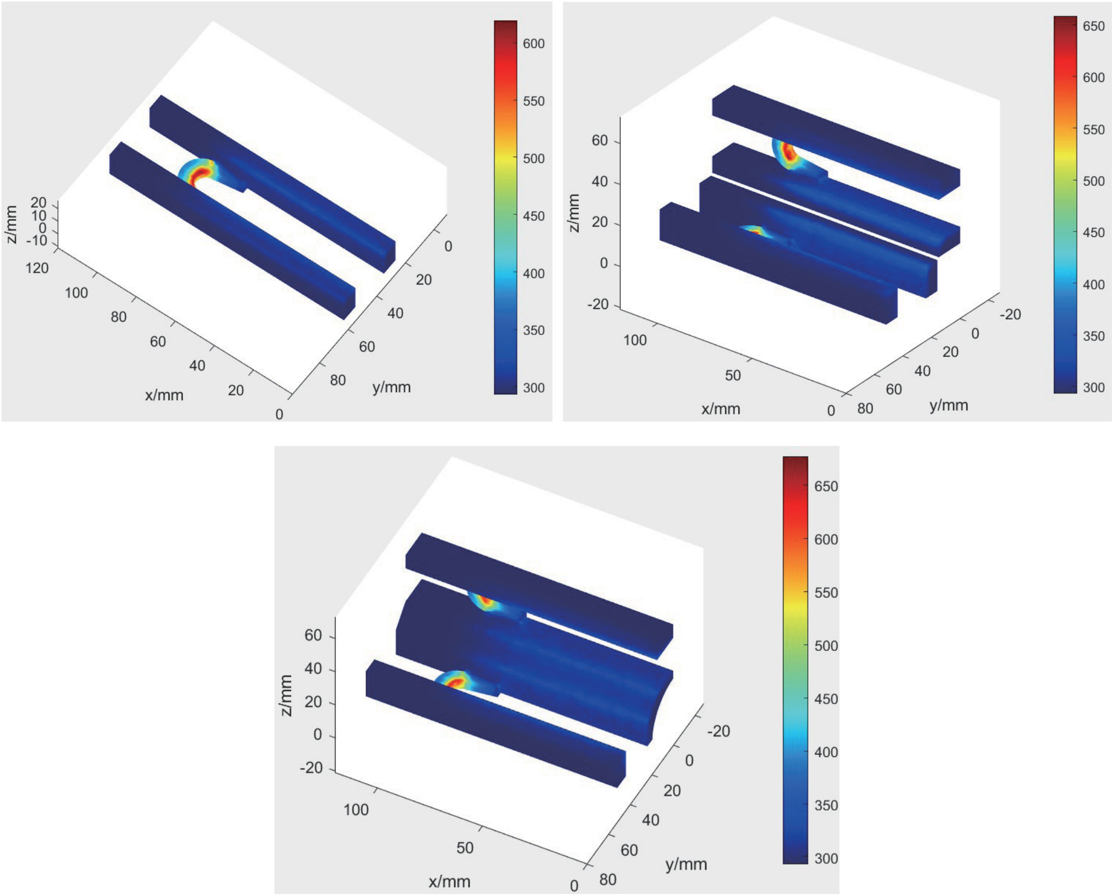

**FIGURE 12**. Temperature distribution at 0.4 ms under different configurations.

### 5.3. Thermal Field Analysis

The conductor temperature distribution at 0.4 ms is shown in Fig. 12. In all three configurations, the maximum temperature is located in the armature throat with values of 619.18 K, 658.64 K, and 677.27 K, respectively. Multi-turn EMRLs generate a larger Joule heat source due to the strong electromagnetic coupling in the conductors between different turns, so the conductor temperature rises faster and higher. The waveform of the maximum temperature inside the conductor over time is shown in Fig. 13. The armature of configuration 1 reaches the melting temperature at 0.86 ms and then begins the isothermal phase transition process. The armatures of configurations 2 and 3 reach melting temperature slightly earlier than configurations 1. The maximum temperatures of the split and integrated rails were close until about 0.72 ms. After that, the maximum temperature of the integrated rail begins to be smaller than that

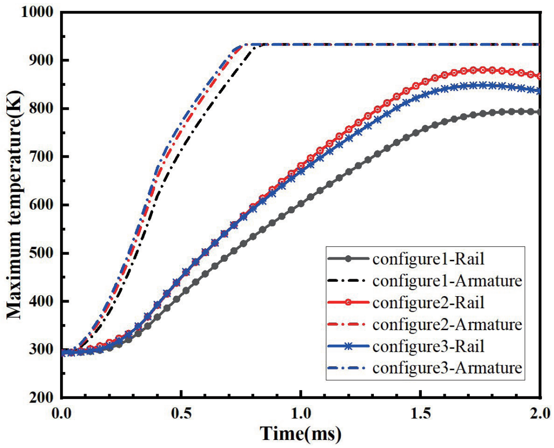

**FIGURE 13**. Waveform of the maximum temperature under different configurations.

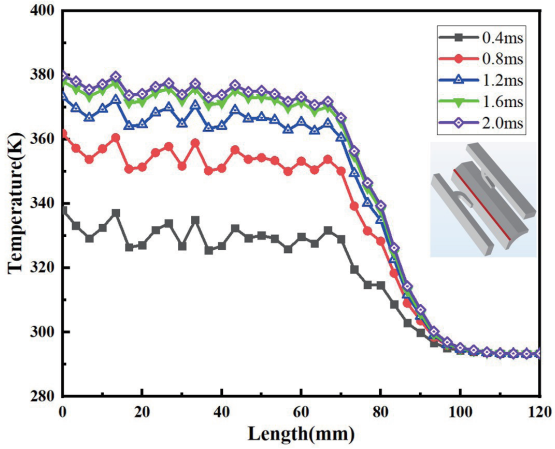

**FIGURE 14**. Rail edges temperature distribution at different times in configuration 3.

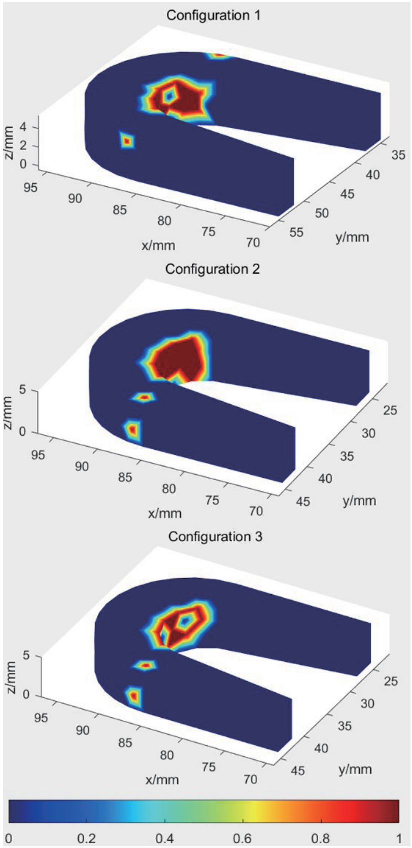

**FIGURE 15**. Comparison of armature ablation at 2 ms in three configurations.

of split rails, and the difference gradually increases, reaching a maximum of 31.75 K. Although the temperature of the multi-turn EMRLs is higher than that of the single-turn, the temperature rise is still within the acceptable range due to the better heat resistance of the copper rail material.

Considering that configuration 3 has better comprehensive electromagnetic and mechanical properties, we further study its temperature field distribution. The temperature of the negative rail edge in configuration 3 over time is shown in Fig. 14. At the armature tail position, the rail edge temperature drops rapidly. And the temperature of the rail edge rises over time. However, the temperature rise of the rail edge gradually slows down, due to the gradual uniformity of the distribution of current. At the same time, the current density is further reduced along the current decline stage, which makes the rail edge temperature at 1.6 ms and 2.0 ms without a large change.

Figure 15 shows the ablation of the armature in three configurations at 2 ms, where red indicates the ablation area, and the material has completed the isothermal phase transition and converted into a liquid state. In the three configurations, the armature has ablation on the throat and both sides of the contact surface, and the armature of the split multi-turn EMRL is the most severely ablated. Relatively speaking, the armature in configuration 3 has good distribution results.

## 6. CONCLUSION

In this paper, the finite element method of tetrahedral elements is used to establish a multi-field coupling model of multi-turn EMRL. The calculation results of the same model under the same conditions are consistent with the software recognized by the industry, and experimental verification is carried out to verify the effectiveness of the model. The main conclusions are: For multi-turn configurations of circumferential array, the magnetic induction intensity of the armature between the different turns is mutually enhanced, and the armature magnetic induction intensity is higher than the single-turn armature magnetic field at the same time. There is a self-shielding effect of the magnetic field in the space region surrounded by the negative rail. The pilot arc structure in the integrated negative rail configuration improves the phenomenon of different current distributions between the positive and negative rails. Compared to single-turn EMRL, the armatures have greater driving forces in the two multi-turn configurations, and the impulse lift rates are about 1/2. Under the two multi-turn configurations, the lateral resultant forces of the two arms of the armature are not zero, and the excessive lateral force difference is not conducive to the launch process and may lead to contact failure, while the lateral force difference in the integrated negative rail configuration is relatively small. Armatures have ablation on both sides of the contact surface and throat, with the most severe ablation in the split negative rail configuration. In contrast, the ablation of the armature in the integrated negative rail configuration is less severe. This paper extends the design ideas of novel multi-turn EMRLs, rather than being limited to the described configurations. By properly distributing the angle of the circular array, EMRL structures such as 6 turns, 8 turns, and even more can be designed. However, this study was performed under the conditions of static armatures. To be more realistic, the model could be improved by taking into account velocity effect in further work.

## ACKNOWLEDGEMENT

This work was supported in part by the CAS "Light of West China" Program under Grant xbzg-zdsys-202317, and in part by the Scientific Instrument Developing Project of the Chinese Academy of Sciences under Grant YJKYYQ20200011, and in part by the Joint fund of Chinese Academy of Sciences under Grant 8091A02, and in part by Institute of Electrical Engineering and the Advanced Electromagnetic Drive Technology, Qilu Zhongke Research Fund Project.

## REFERENCES

[1] Hundertmark, S., G. Vincent, F. Schubert, and J. Urban, "The NGL-60 railgun," *IEEE Transactions on Plasma Science*, Vol. 47, No. 7, 3327–3330, Jul. 2019.

[2] Fair, H. D., "The science and technology of electric launch," *IEEE Transactions on Magnetics*, Vol. 37, No. 1, 25–32, Jan. 2001.

[3] Zhang, B., Y. Kou, K. Jin, and X. Zheng, "A multi-field coupling model for the magnetic-thermal-structural analysis in the electromagnetic rail launch," *Journal of Magnetism and Magnetic Materials*, Vol. 519, 167495, Feb. 2021.

[4] Angeli, M. and E. Cardelli, "Electro-thermal behavior of solid armatures," *IEEE Transactions on Magnetics*, Vol. 35, No. 1, 47–52, Jan. 1999.

[5] Sun, J., J. Cheng, Q. Wang, L. Xiong, Y. Cong, and Y. Wang, "Numerical simulation of melt-wave erosion in 2-D solid armature," *IEEE Transactions on Plasma Science*, Vol. 50, No. 4, 1032–1039, Apr. 2022.

[6] Li, S., J. Li, S. Xia, Q. Zhang, and P. Liu, "Phase division and critical point definition of electromagnetic railgun sliding contact state," *IEEE Transactions on Plasma Science*, Vol. 47, No. 5, 2399–2403, May 2019.

[7] Bayati, M. S. and A. Keshtkar, "Novel study of the rail's geometry in the electromagnetic launcher," *IEEE Transactions on Plasma Science*, Vol. 43, No. 5, 1652–1656, May 2015.

[8] Sun, J., J. Cheng, Q. Wang, L. Xiong, Y. Cong, and Y. Wang, "Research on arc suppression parameter matching of augmented electromagnetic launcher," *IEEE Transactions on Plasma Science*, Vol. 49, No. 12, 3988–3993, Dec. 2021.

[9] Bayati, M. S., A. Keshtkar, and A. Keshtkar, "Transition study of current distribution and maximum current density in railgun by 3-D FEM-IEM," *IEEE Transactions on Plasma Science*, Vol. 39, No. 1, 13–17, Jan. 2011.

[10] Bayati, M. S., A. Keshtkar, and A. Keshtkar, "Thermal computation in railgun by hybrid time domain technique 3-D-FEM-IEM," *IEEE Transactions on Plasma Science*, Vol. 39, No. 1, 18–21, Jan. 2011.

[11] Pang, Z., H. Wang, H. Wang, and L. Zhang, "Analysis of current and magnetic field distributions in rail launcher with peaceman-rachford finite-difference method," *IEEE Transactions on Plasma Science*, Vol. 40, No. 10, 2717–2722, Oct. 2012.

[12] Gong, F. and C. Weng, "3-D numerical study of meltwave erosion in solid armature railgun," *High Voltage Engineering*, Vol. 40, No. 7, 2245–2250, 2014.

[13] Hsieh, K., "A lagrangian formulation for mechanically, thermally coupled electromagnetic diffusive processes with moving conductors," *IEEE Transactions on Magnetics*, Vol. 31, No. 1, 604–609, Jan. 1995.

[14] Shatoff, H., D. A. Pearson, and A. E. Kull, "Simulation of dynamic armature motion in a railgun with coupling of electromagnetic, thermal and structural effects using shifted finite element fields," in *2005 IEEE Pulsed Power Conference*, 253–256, 2005.

[15] Lin, Q.-H. and B.-M. Li, "Numerical simulation of interior ballistic process of railgun based on the multi-field coupled model," *Defence Technology*, Vol. 12, No. 2, 101–105, Apr. 2016.

[16] Bayati, M. S., A. Keshtkar, and S. V. A.-D. Makki, "Analyzing the current distribution, magnetic field and inductance gradient at the circular rail in comparison to rectangular rail," in *2012 16th International Symposium on Electromagnetic Launch Technology*, 1–5, Beijing, China, May 2012.

[17] Stefani, F., R. Merrill, and T. Watt, "Numerical modeling of melt-wave erosion in two-dimensional block armatures," *IEEE Transactions on Magnetics*, Vol. 41, No. 1, 437–441, Jan. 2005.